

Dielectric Behavior of α -Ag₂WO₄ and its Huge Dielectric Loss Tangent

Natalia Jacomaci^{a*}, Euripedes Silva Junior^b, Fernando Modesto Borges de Oliveira^b, Elson Longo^b,
Maria Aparecida Zaghete^b

^aInstituto de Química, Universidade Estadual Paulista (Unesp), 14800-060, Araraquara, SP, Brasil

^bDepartamento de Química, Universidade Federal de São Carlos (UFSCar), 13565-905, São Carlos, SP, Brasil

Received: January 21, 2019; Revised: May 08, 2019; Accepted: June 29, 2019

The microwave-assisted hydrothermal method was used to obtain α -Ag₂WO₄. Rietveld refinement confirmed that α -Ag₂WO₄ is stable in the orthorhombic phase, without secondary phase. However, field-effect scanning electron microscope analysis showed that α -Ag₂WO₄ nanorods surfaces contain silver nanoparticles, confirmed by the X-ray photoelectron spectroscopy by the peak observed at 374.39 eV. In addition to metallic Ag, other Ag oxidation states were also observed on the surface. Hence, Ag (I) as Ag₂O and Ag (I) as Ag₂WO₄ also were identified. DC measurements exhibited a high capacity of charge storage, nevertheless, with a large loss tangent (0.12 μ C.cm⁻².V⁻¹) and no residual polarization for the voltage range between -100 V and +100 V. AC measurements at frequencies less than 275 Hz, revealed that ionic polarization is dominant, whereas at frequencies higher than 275 Hz, the electronic behavior predominates. The potential of electromagnetic energy conversion in thermal was observed from loss tangent analysis.

Keywords: Silver tungstate nanorods, dielectric behavior, ionic and electronic polarization.

1. Introduction

Tungsten-silver materials are known to exhibit very good erosion resistance properties in low voltage. However, their use as arcing contacts in circuit breakers is limited when exposed to harsh working environments because of the ease with which they form oxides on the surface, thereby leading to increased contact resistance¹⁻⁵. In addition, the thermodynamic instability of tungsten-silver materials reduces their usefulness at high temperatures near electric arcing regions^{1,6}, because this might result in the formation of different phases with distinct physical and chemical properties, such as silver tungstates (Ag₂WO₄ and AgWO₃)⁶, silver oxide (AgO)⁷ and tungsten oxides (WO_x)^{4,6-8}, which would degrade the circuit breaker performance^{1,6}. Thereby, the oxidation of tungsten-silver compounds become a laborious process, as well as its resistive behavior, since silver is normally free from oxides at elevated temperatures, leading to breaking of structural arrangement of primitive structure^{4,7}. However, interesting physical and chemical properties of the less stable structures may arise, since these exhibit unique properties that are distinct from those of the thermodynamically stable phase⁸⁻¹⁰. In this regard, in recent years, several researchers have reported many interesting potential applications of transition-metal tungstates, because they exhibit a special symmetry property caused by spontaneous polarization, which in turn implies ferroelectric behavior, ionic conductivity and photoluminescence¹¹⁻¹⁴.

Among transition metal tungstates, silver tungstate (Ag₂WO₄) has attracted the attention of the scientific and technological community because of its chemical stability, easy synthesis¹⁵, and multifunctional applications, which include catalysis^{16,17}, photocatalysis¹⁸⁻²⁰, electrocatalysis²¹, photoluminescence²²⁻²⁴, photoswitches²⁵, chemical sensing^{25,26}, and antibacterial agents²⁷⁻²⁹.

From the structural point of view, Ag₂WO₄ can be found in three main crystallographic forms: α -Ag₂WO₄ (orthorhombic; *Pn2n*), β -Ag₂WO₄ (hexagonal; *P6₃* or *P6₃/m*), and γ -Ag₂WO₄ (cubic, *Fd3m*)³⁰⁻³². Orthorhombic is the most stable, and its chemical stability is retained up to ~347 °C, while β - and γ -Ag₂WO₄ are metastable, being easily transformed to α -Ag₂WO₄ under heating at 187°C and 257 °C, respectively³⁰. Regardless of the crystallographic phase, the lattice crystal of Ag₂WO₄ comprises a system of building-block units formed by a series of allotropic forms of [WO₆] and [AgO_y] clusters^{15,22-24,29}. Since the physical and chemical properties are heavily dependent on structural features, those properties of each Ag₂WO₄ structure will depend on the order-disorder relationship between these clusters, since a symmetry break induced by strain, stress, and distortions within the Ag₂WO₄ crystal lattice may create new and distinct structures, and thereby give rise to new and different properties^{15,23,33}. According to the published literature, these structural variations are a consequence of the synthesis method and experimental conditions (temperature, processing time, solvent, heating source, pH, template, electron beam exposure, etc.)^{10,11,16,29,33}.

*e-mail: natalia.jacomaci@unesp.br

The preparation of α -Ag₂WO₄ has been successfully carried out by several methods which include solid state reaction³⁴⁻³⁶, co-precipitation^{22,37-39}, laser ablation in liquid (LAL)¹⁸, hydrothermal^{19,21-27,29,40-42}, sonochemical^{22,28} and microemulsion²² methods. Despite the large number of synthesis methods available, it has been a challenge to obtain a fully stable α -Ag₂WO₄ structure. Nevertheless, in recent years, promising studies^{15,24,27,29,39,42-44} exploring the chemical and structural stability of α -Ag₂WO₄ nanostructures under electron beam and UV light exposure, revealed that interfaces created between Ag and α -Ag₂WO₄ lead to improvements in the properties of the nanocomposites that are formed.

Lastly, a large number of studies about α -Ag₂WO₄ has been published reporting only the structural description, optical properties and the growth mechanisms, which risen from different synthesis methods. However, in this work we concentrate on the structural and microstructural analysis of α -Ag₂WO₄, that were crucial for a better understanding of its structural stability and AC/DC electrical properties which show up an interesting potential as electrothermal energy conversion.

2. Experimental Details

2.1 Synthesis

The α -Ag₂WO₄ nanostructures were prepared by a microwave-assisted hydrothermal (MAH) method. The first synthesis step consists of the preparation of two solutions, A and B, both of which contain 0.25 g of polyvinylpyrrolidone-40 (PVP40 - Sigma Aldrich) dissolved in 50 mL of deionized water by mechanical stirring. After complete surfactant solubilization, 1 mmol of Na₂WO₄·2H₂O (99% Alfa Aesar) and 2 mmol of AgNO₃ (99% Synth) were added to solution A and B, respectively, under continuous stirring. Once precursor solubilization was observed, both solutions were mixed together and transferred to a Teflon vessel sealed with a manometer to monitoring the hydrothermal pressure. The system was heated in a microwave oven furnace (PANASONIC, 2.45 GHz and 800 W) at 160 °C with a heating rate of 10 °C·min⁻¹ for 1 h under constant pressure (~7 bar). Afterwards, the particle precipitate was separated via centrifugation (10.000 rpm) and washed several times with water and acetone to eliminate Na⁺ and organic residues. Lastly, the precipitate was dried at 70 °C in a desiccator for 24 h.

2.2 Characterization techniques

The X-ray powder diffraction technique (XRD) was employed to investigate the structural ordering at long-range of α -Ag₂WO₄, using a diffractometer (Rigaku-DMAX/2500PC) with Cu-K α radiation ($\lambda = 1.5406 \text{ \AA}$) in the 2θ range from 10° to 100° with a scanning speed of 1°·min⁻¹ and a step of 0.02°. To obtain more information about the α -Ag₂WO₄ crystal structure, Rietveld refinement⁴⁵ was employed using TOPAS-Academic V6 software from the inorganic crystal structure database crystallographic information file ICSD no. 4165³².

The parameters refined were scale factor, background, sample shift, crystal lattice, and peak broadening anisotropic, preferential orientation, atomic position, and isotropic thermal parameters. The peak profile was modelled by fundamentals parameters approach.⁴⁶ The anisotropic broadening of the sample was modelled using the Stephens's model.⁴⁷ The structure established by statistics parameters R_{wp} , R_{exp} , R_{Bragg} , Goodness (χ^2) and good visual adjust both experimentally fitting and theoretical patterns.⁴⁸

The shapes and sizes of the α -Ag₂WO₄ nanostructures were investigated using a field-emission scanning electron microscope (FE-SEM) (Carl Zeiss - Supra 35-VP) operating at 2 kV.

The chemical environment of the α -Ag₂WO₄ was investigated with the X-ray photoelectron spectroscopy (XPS) technique. XPS spectra were collected using a commercial spectrometer (UNI-SPECS-UHV) using the Al K α line ($h\nu = 1486.7 \text{ eV}$) with its analyzer pass energy set up to 50 eV. The inelastic noise of the C 1s, O 1s, W 4f, and Ag 3d spectra and the Auger Ag MNN peak were subtracted using Shirley's method⁴⁹. The binding energies were corrected using the hydrocarbon component of adventitious carbon fixed at 285.0 eV. In order to perform the direct current (DC) and alternating current (AC) measurements, two cylindrical pellets with an area of 182 μm^2 and a thickness of 1.98 mm were obtained by isostatic pressing at 200 MPa. The electrical contacts were fabricated by depositing gold on both faces of the pellets that had been covered with Kapton[®] tape to avoid electrical conduction between them. The DC measurements were acquired with a Radiant Precision Multiferroic Tester (Radiant Technologies Ltd., Albuquerque, NM), while the AC measurements were carried out by a potentiostat/galvanostat (PGSTAT 128N-Metrohm Autolab). The pellets were stored in a chamber under mechanical vacuum pumping and at room temperature. Impedance analysis as well as spectrum simulations were performed by electrochemical impedance spectroscopy spectrum analyzer software (EIS-SA)⁵⁰.

3. Results and Discussion

3.1 XRD structural analysis

Figure 1 shows the indexation planes of X-ray diffraction pattern of the MAH-produced α -Ag₂WO₄. As can be observed in the diffraction pattern, all diffraction peaks are in good agreement with the orthorhombic Ag₂WO₄ structure (space group: $Pn2n$) according to ICSD no. 4165³² and the literature^{19,21-27,29,40-42}, without any secondary phase. The profile of the diffraction pattern reveals that α -Ag₂WO₄ materials exhibit a high degree of crystallinity, since the peak reflections are intense and sharp. Also, to observe the occurrence of anisotropic growth of the crystal, evidence by intensity of the (231) reflection is relatively higher than that of the intensity that if the others planes, this results in anisotropic microstrain and orientation preferential effects that are corrected by Rietveld refinement.

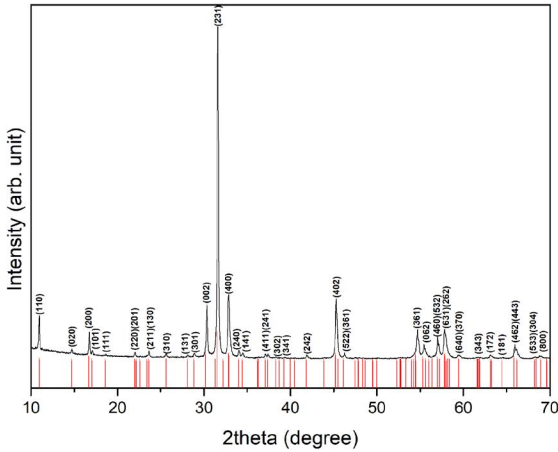


Figure 1. X-ray diffraction patterns of the α -Ag₂WO₄ microcrystals prepared at 160°C for 1 h the MAH method. Red lines are the positions of the data from ICSD no. 4165 for this phase.

Figure 2 shows curve-fitting carried out with TOPAS-Academic software and the Rietveld method. The good overlap between experimental (observed pattern) and standard (theoretical pattern) profiles (see Fig. 2) and the values of the statistical parameters R_{wp} , R_{exp} , and *Goodness* (χ^2) shown in Table 1 confirm the good quality of the refinement from the Rietveld method, since they are in agreement with values reported in literature^{15,22-24} for the α -Ag₂WO₄ structure.

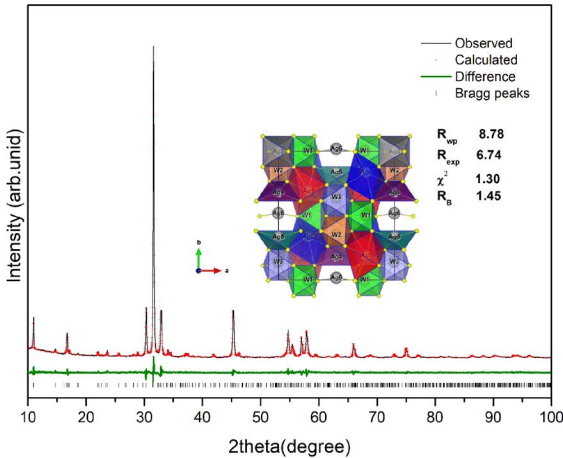


Figure 2. Diffraction pattern from Rietveld refinement analysis of the α -Ag₂WO₄ structure processed by the MAH method at 160 °C for 1h.

Pristine α -Ag₂WO₄ structures are formed by a complex network of clusters of [WO₆] and [AgO_y] ($y=2, 4, 6$ or 7), where the polyhedral [WO₆] exhibit octahedral geometry with symmetry group O_h , while the [AgO_y] clusters are formed according to Ag atoms coordination^{22,24,29,32}.

Cavalcante et al.²² and Longo et al.²⁴ published a detailed investigation of the electronic structure of α -Ag₂WO₄ from experimental and theoretical approaches; they reported that in the [WO₆] polyhedral clusters, the occupancy sites of the W atoms can be found in three distinct arrangements (W1, W2, and W3), each of which is coordinated to six O atoms. On the other hand, the [AgO_y] clusters consist of six different Ag atoms (Ag1, Ag2, Ag3, Ag4, Ag5, and Ag6) that occupy different sites in the lattice. Therefore, Ag1 and Ag2 atoms are coordinated to seven O atoms as delta-hedral polyhedral [AgO₇] with symmetry group D_{5h} , while Ag3 atoms are hexacoordinated to six O atoms, resulting in [AgO₆] distorted octahedral polyhedral of symmetry group O_h . Moreover, Ag4 and Ag5 are coordinated to four O atoms in the form of [AgO₄] tetrahedral polyhedra with symmetry group T_d . Lastly, the Ag6 atoms are coordinated by two O atoms, which results in [AgO₂] angular polyhedra of symmetry group C_{2v} . As can be observed in Table 1, the structural data from Rietveld refinement analyses revealed that some displacements in the atomic coordinates of the W and Ag atoms promoted changes in the lattice parameters b and c , and thereby unit cell shrinkage, leading to the unit cell shrinkage, once the volume of unit cell of the α -Ag₂WO₄ obtained by MAH was of 771.2000 (\AA^3), while for the α -Ag₂WO₄ (ICSD no. 4165) is of 775.5596 (\AA^3).

Confirming this behavior, recent studies reported that cluster units formed by [WO₆] and AgO_y ($y=2, 4, 6$, and 7) display a degree of distortion at short-, medium-, and long-range generated by changes in bond angles and lengths, which vary for different synthesis methods, leading to changes in the physical and chemical properties such as photoluminescence²²⁻²⁴, bacterial activity^{24,29,44}, and gas sensing^{26,42}. Based on this observation, the α -Ag₂WO₄ obtained here by the MAH method may exhibit interesting and unique physical and chemical properties that can be useful for technological applications.

3.2 FE-SEM analyses

The shape and size of the α -Ag₂WO₄ structure produced by the MAH method is exhibited in Fig. 3. As can be observed by FE-SEM analysis, α -Ag₂WO₄ material is formed by an agglomerate of microcrystals with a rod-like elongated shape and an average length of 1.4 μm . Figs. 3 (c, d) are high magnification FE-SEM images of the sample with a magnification of 10^5 . It is possible to clearly observe in Figs. 3 (c, d) the presence of some silver metal dots on the surfaces of the nanorods; we believe that these were created by the MAH method and not grown by electron beam irradiation, since the acceleration voltage employed in FE-SEM analysis was low (2 kV), as was the exposure time of the nanostructures to the electron beam.

Table 1. Lattice parameters (a, b, c), coordinates of the atoms' positions (x, y, z), and sites of α -Ag₂WO₄ nanostructures and statistical parameters obtained from the Rietveld refinement method using TOPAS-Academic software.

α-Ag₂WO₄ - Pn2n-crystalline structure				
This work(experimental)				
sites and coordinates atomics				
Atoms	sites	x	y	z
W1	4c	0.25636	0	0.51147
W2	2b	0	0.84764	0.5
W3	2b	0	0.14040	0.5
Ag1	4c	0.75974	0.18827	0.96455
Ag2	4c	0.24301	0.83408	0.01478
Ag3	2a	0	0.99411	0
Ag4	2a	0	0.67684	0
Ag5	2a	0	0.33292	0
Ag6	2b	0	0.51671	0.5
O1	4c	0.368	0.612	0.195
O2	4c	0.368	0.378	0.188
O3	4c	0.419	0.735	0.815
O4	4c	0.425	0.263	0.792
O5	4c	0.162	0.494	0.282
O6	4c	0.414	0.496	0.847
lattice parfameters				
a(Å³)	b(Å³)	c(Å³)	volume (Å³)	density (Å³)
10.89	12.01	5.89	771.2000	7.98
statistical parameters				
R_{wp}	R_{exp}	R_{Bragg}	gof	
8,78	6,74	1,45	1,30	
ICSD no. 4165⁴⁹(theoretical)				
sites and coordinates atomics				
Atoms	sites	x	y	z
W1	4c	0.25400	0	0.52550
W2	2b	0	0.84764	0.50000
W3	2b	0	0.13800	0.50000
Ag1	4c	0.75090	0.17110	0.98770
Ag2	4c	0.23490	0.81760	0.00920
Ag3	2a	0	0.98720	0
Ag4	2a	0	0.65310	0
Ag5	2a	0	0.31480	0
Ag6	2b	0	0.50920	0.50000
O1	4c	0.36800	0.61200	0.19500
O2	4c	0.36800	0.37800	0.18800
O3	4c	0.41900	0.73500	0.81500
O4	4c	0.42500	0.26300	0.79200
O5	4c	0.16200	0.49400	0.28200
O6	4c	0.41400	0.49600	0.84700
lattice parameters				
a (Å³)	b (Å³)	c (Å³)	volume (Å³)	density (Å³)
10.8900	12.0300	5.9200	775.5596	7.94

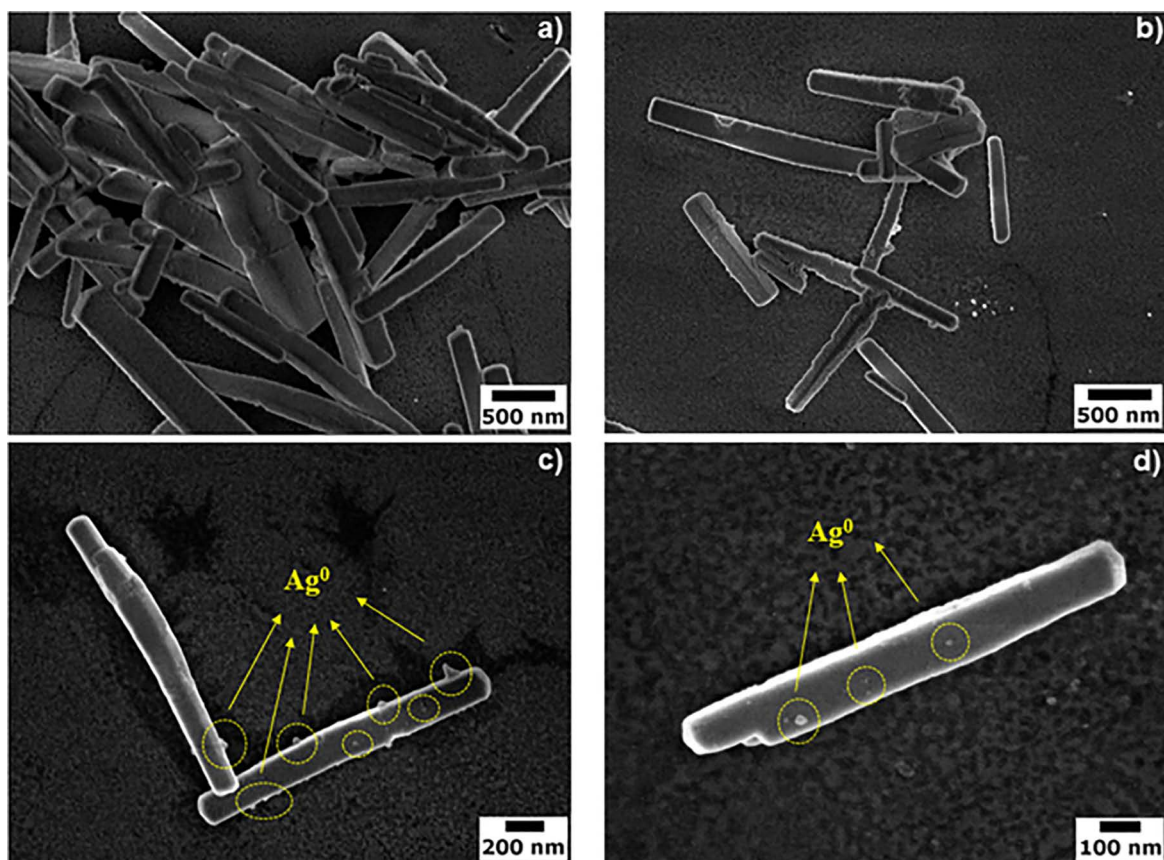


Figure 3. FE-SEM image of the α -Ag₂WO₄ nanorods processed by the MAH method at 160 °C for 1h.

3.3 XPS surface analysis

XPS was carried out on the α -Ag₂WO₄ material in order to provide additional information about the surface composition as well as to unravel the chemical environment, since the XRD results pointed to unit cell shrinkage. The survey spectrum (Fig. 4a) and Table 2 exhibit the microanalysis of α -Ag₂WO₄ nanorods, where it is possible to identify only the presence of C, Ag, W, and O atoms, indicating the high purity of sample. It is worth mentioning that the carbon presence at 285 eV in the survey spectrum at 285 is due to the hydrocarbon component of adventitious carbon employed to correct the binding energies (BEs). Microanalysis of the composition of Ag, W, and O atoms on the α -Ag₂WO₄ surface material was carried out using the atomic fractions (At.%, see fifth column in Table 2) measured by depth-profiling XPS from the ratio of peak areas corrected by the sensitivity factors (Scofield)

for each element. High-resolution XPS spectra of O 1s, Ag 3d, and W 4f are presented in Fig. 4 (b-d). The core-level binding energies of O 1s in the spectrum (Fig. 4b) display an asymmetric peak revealing the presence of different O species in the sample. Next, from a fitting analysis, the O 1s core-level spectrum was deconvoluted into components at 529.76 eV and 531.40 eV, which are assigned to the oxygen in Ag-O and W-O, respectively^{15,37,51}.

Moreover, the additional deconvoluted component at 533.46 eV can be ascribed to oxygen from O=C=O species chemisorbed onto the surface¹⁵. The W 4f core-level spectrum shown in Fig. 4c exhibits well-resolved spin-orbit split doublets peaks related to the W 4f_{5/2} and W 4f_{7/2} states. However, the deconvoluted W 4f peak gives clear evidence of other W oxidation states because of the peak profile, so that doublet W 4f states at high BEs can be related to the W⁶⁺ oxidation state, while those at low energy are related to the W⁵⁺ oxidation state⁵²⁻⁵⁴.

Table 2. Position, area, FWHM, and atomic fraction (At.%) values of the C, Ag, W, and O peaks for a typical XPS survey spectrum of α -Ag₂WO₄ obtained by the MAH method.

Peaks	Position (eV)	Area (%)	FWHM	At %
C 1s	285	2189.70	2.31	57.71
W 4f	247.98	1118.65	4.68	1.81
O 1s	530.88	3285.50	5.06	29.57
Ag 3d	368.35	7420.11	2.24	10.85

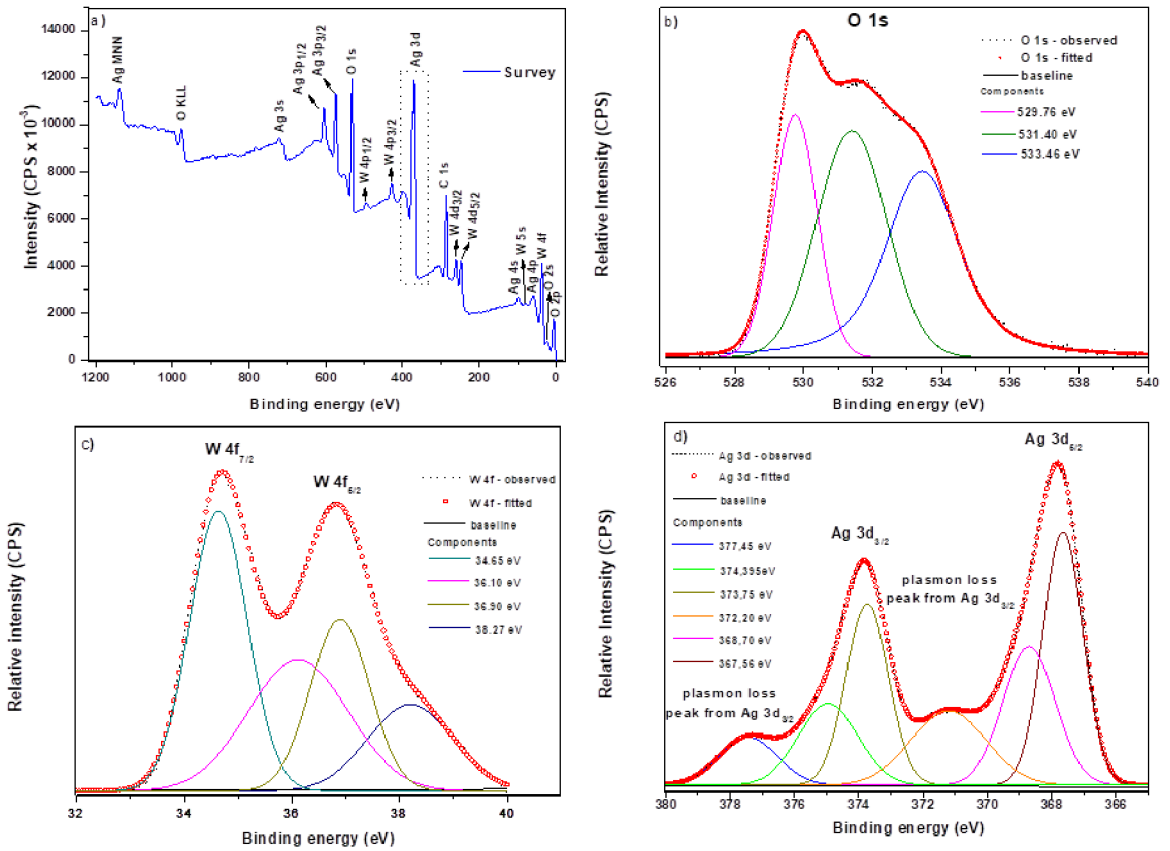


Figure 4. XPS survey spectrum of α - Ag_2WO_4 processed by the MAH method. (a) High-resolution XPS spectra of the α - Ag_2WO_4 sample; (b) O 1s, (c) W 4f and (d) Ag 3d regions.

Therefore, the deconvoluted components at 38.27 eV ($\text{W } 4f_{5/2}$) and 36.10 eV ($\text{W } 4f_{7/2}$) are attributed to the W^{6+} as Ag_2WO_4 compound, while the low BEs at 36.90 eV ($\text{W } 4f_{5/2}$) and 34.6 eV ($\text{W } 4f_{7/2}$) are assigned to the W^{5+} as $\text{Ag}_2\text{WO}_{4-x}$ because of the oxygen vacancies on the surface. The Ag 3d doublet (Ag $3d_{3/2}$ and Ag $3d_{5/2}$), observed in the Ag 3d core-level spectrum (Fig. 4d), exhibited a remarkable peak asymmetry due to the plasmon loss effect^{55,56}, suggesting the presence of Ag metal on the α - Ag_2WO_4 surface. This observation is in good agreement with the FE-SEM (Fig. 3c,d) results, confirming thus the presence of Ag metal (Ag^0) on the surfaces of the α - Ag_2WO_4 nanorods. The asymmetry of the Ag 3d core-level binding energies definitely suggests the existence of more than one silver oxidation state⁵⁷, which can be supported by the Ag 3d deconvoluted peaks from the fitting analysis. Therefore, the deconvoluted components at 367.6 eV (Ag $3d_{3/2}$) and 373.75 eV (Ag $3d_{5/2}$) are assigned to the existence of Ag^+ as surface Ag_2O ⁵⁸. The plasmon loss effect manifests itself as satellites peaks at larger BEs because the energy transfer of the photoelectron reduces its kinetic energy; i.e., the binding energy should be larger^{52,53}. Therefore, the peaks observed at 372.20 eV and 377.45 eV correspond to the surface-plasmon loss.

Ag^0 in metallic form on the α - Ag_2WO_4 surface was assumed to be the cause of the peak observed at 374.39 eV (Ag $3d_{3/2}$)⁵⁹, while the peak observed at 368.70 eV (Ag $3d_{5/2}$) indicates the existence of Ag^+ in the form of the Ag_2WO_4 compound^{15,52}.

Thus, from the Ag 3d core-level XPS spectrum results we conclude that the unit cell shrinkage observed by the Rietveld refinement method, might be associated to silver vacancies on the bulk α - Ag_2WO_4 generated by MAH method, which have migrated toward nanorods surface.

3.4 DC/AC analyses

Electrical analyses based on DC bias are shown in Fig. 5, in the form of I-V curves, Fig. 5a, verifies the Ohmic behavior of the α - Ag_2WO_4 material; in this specific geometry, it presents a resistance of $5.82 \times 10^7 \Omega$ and a resistivity of $5.34 \times 10^8 \Omega \cdot \text{m}$. The electrical polarization measurement in Fig. 5b (electric displacement), yielded very large values, even higher than BaTiO_3 composites⁶⁰; however, as will be seen below, the loss tangent is also very large, indicating poor storage properties. Although α - Ag_2WO_4 is a ferroelectric material in this range of voltage (-100 V to 100 V), no residual polarization is seen.

Figure 6 shows the Nyquist and Bode plots measured from 30 mHz to 1 MHz with a wave amplitude of 350 mV, as well as the proposed equivalent circuit (EC) and its respective profile, which can be compared with experimental curves. The EC chosen was the same one proposed by Cole⁶¹; however, as α -Ag₂WO₄ is a semiconductor, a resistive element was added in parallel. Thus, from the EC, the C1 parameter corresponds to electronic polarization, C2 corresponds to ionic polarization, and the constant phase-angle element (CPE) is related to the non-ideal capacitance of ionic dipoles, R1 is the contact resistance, and R2 is the resistance belonging to α -Ag₂WO₄. All parameters were calculated by EIS SA software and are summarized in Table 3.

Table 3. Equivalent circuit parameters for α -Ag₂WO₄.

Parameters	Values
R_1	2.4 K Ω
R_2	6.1 M Ω
C_1	7.9 pF
C_2	19.7 nF
Y_{oi}^{-1}	$1.2 \cdot 10^{-10} \text{S} \cdot \Omega^{-1}$
n_1	0,52

In order to calculate the resultant circuit capacitance, it is necessary to know the effective capacitance of the CPE $[(Z(\text{CPE}) = Y_0^{-1}(j\omega)^{-n}]$, which can be obtained by: $C_{ef} = Y_0(2\pi f'_m)^{n-1}$ where f'_m corresponds to the frequency whose Z'' has the highest value⁶². By placing the f'_m value, indicated in Fig. 6a, into the C_{ef} equation, we obtain a capacitance of 3.42pF. The sum of capacitance phenomena, resulting from ionic dipoles, C_2 plus C_{ef} , is equal approximately to 3.42 pF, which is the same magnitude as the capacitance derived from electronic polarization. Although C_{ef} from non-ideal capacitance had decrease equivalent ionic capacitance, it is not predominant at overall capacitance this assumption can be confirmed in Fig. 6b.

The phase difference of 90° represents an ideal capacitance, and therefore, the predominance of electronic polarization. Otherwise, as shown by the Nyquist plot, up to 275 Hz, $|Z''|$ is quite similar to $|Z'|$, denoting an ideal capacitance. At frequencies below 275 Hz, deviations from ideal capacitance can be seen; hence, non-ideal phenomena are occurring at those frequencies. By performing simulations of the EC at frequencies from 1 μ Hz to 100 MHz, it is possible to obtain information at frequencies that cannot be provided by the equipment used in this study; obviously, this is only true if material electrical behavior it is modeling by the same EC for all frequencies within the range being studied.

Figure 7a shows the simulated capacitance and loss tangent of α -Ag₂WO₄. To 1 μ Hz the simulating capacitance corresponds to $1.3 \times 10^{-2} \mu\text{F}$, which is the same magnitude as C_2 ($1.97 \times 10^{-2} \mu\text{F}$). By multiplying the angular coefficient of the polarization curve in Fig.5b, times $1.82 \text{ cm}^2 \times 0.35\text{V}$, a capacitance value of $7.64 \times 10^{-2} \mu\text{F}$ will be obtained again, the same magnitude as C_2 . It can be concluded that the EC at low frequencies matches very well with the DC results; moreover, at low frequencies, capacitive phenomena come from ionic polarization. Despite this, α -Ag₂WO₄ is not a good capacitor since it has a very large loss tangent that in turn is due to the non-ideal polarization behavior. The equivalent capacitance from the EC is 11 pF ($3.42\text{pF} + C_1$), this capacitance value occurs at the frequency at which electronic and ionic polarization work together. Graphically, the equivalent capacitance $C'(f'_m)$ in Fig. 6b corresponds to 10.4 pF; confirming that EC proposed is reasonably good. At frequencies below f'_m , ionic polarization predominates, while at higher frequencies, the electronic polarization stands out. The constant region of capacitance in Fig. 6b is relative to electronic polarization; the experimental value is 8.2 pF, and the calculated value is 7.9 pF. The large loss tangent of α -Ag₂WO₄ at low frequencies is comparable to the loss tangent of shown at 0 °C and 9.38 GHz. Thus, at 1 μ Hz there is a strong conversion of electromagnetic energy to heat.

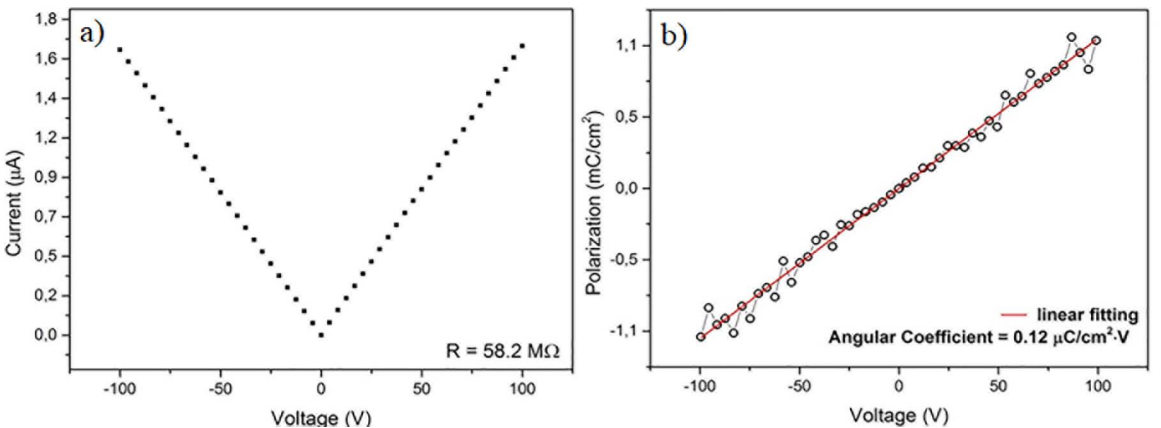


Figure 5. (a) I-V characteristic curve and (b) polarization as a function of voltage in α -Ag₂WO₄ obtained by DC bias measurements.

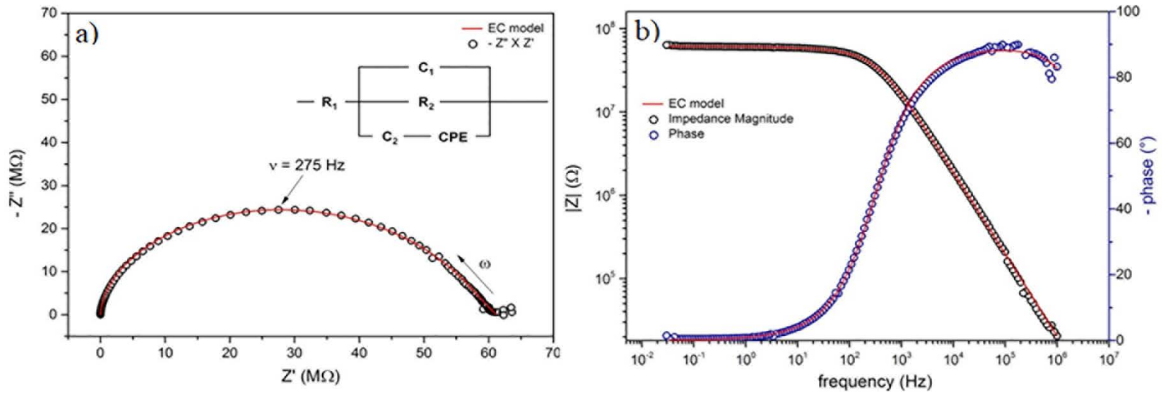


Figure 6. The semicircle represents the experimental data, and the red solid line comes from the fitting of the EC (a). The black and blue semicircles are experimental data for the impedance magnitude and phase, and the red solid line shows the EC fitting (b).

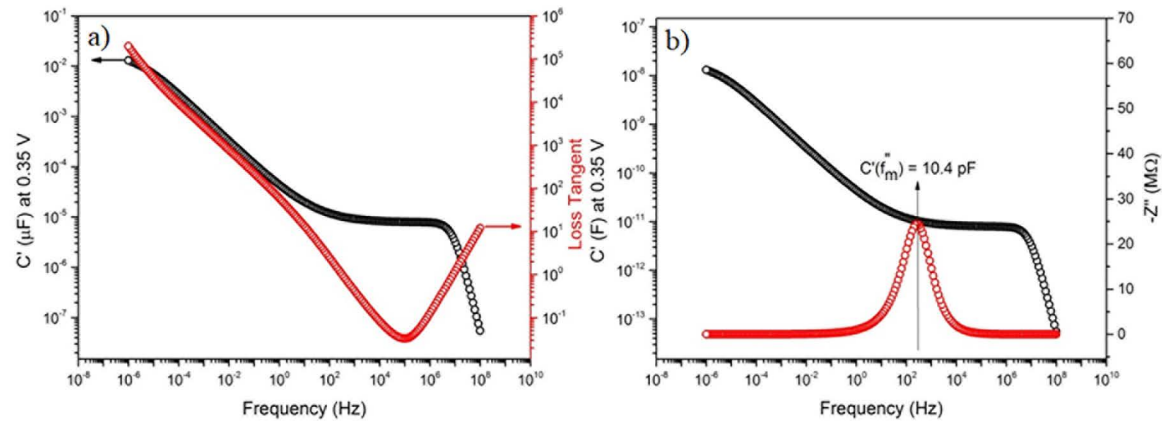


Figure 7. Simulation of capacitance and loss tangent (a) and capacitance and complex impedance versus frequency in the range from 1 μ Hz to 100 MHz (b).

4. Conclusions

The refinement of α - Ag_2WO_4 structures obtained by MAH showed displacement of the atomic coordinates of the W and Ag atoms. This, in turn, changes the b and c lattice parameters, resulting in unit cell shrinkage. FE-SEM analysis of this material showed a morphology consisting of rod-like microcrystals with an average length of 1.4 μm . At high magnification, the presence of some silver metal dots was observed on the surface of the nanorods, this assumption can be supported by the contrast difference between silver nanoparticles (Ag^0) and nanorods surface. XPS measurements reinforced the FE-SEM observation since the Ag 3d doublet (Ag 3d_{3/2} and Ag 3d_{5/2}) observed in the Ag 3d core-level spectrum exhibited a remarkably asymmetric peak due to the plasmon loss effect, suggesting the presence of Ag metal on the α - Ag_2WO_4 surface. I-V measurements it was register the ohmic behavior of the α - Ag_2WO_4 nanorods with characteristic resistance ($\sim 58 \text{ M}\Omega$) of a semiconductor. Polarization measurements found no residual polarization in the voltage range employed. However, α - Ag_2WO_4 shows a very large polarization coefficient of 0.12 $\mu\text{C}/(\text{cm}^2\cdot\text{V})$.

Finally, from AC electrical measurements, it was seen that at frequencies less than 275 Hz, there is a predominance of ionic behavior; at frequencies higher than that, electronic behavior prevails. Overall capacitance, obtained by EC fitting, is approximately 10 pF.

5. Acknowledgements

This work was supported by the Brazilian research agency CAPES and FAPESP (CEPID/CDMF - process number 2013/07296-2).

6. References

1. Kesim MT, Yu H, Sun Y, Aindow M, Alpay SP. Corrosion, oxidation, erosion and performance of Ag/W-based circuit breaker contacts: A review. *Corrosion Science*. 2018;135:12-34.
2. Leung CH, Kim H. A Comparison of Ag/W, Ag/WC, and Ag/Mo Electrical Contacts. *IEEE Transactions on Components, Hybrids, and Manufacturing Technology*. 1984;7(1):69-75.
3. Ray N, Kempf B, Wiehl G, Mützel T, Heringhaus F, Froyen L, et al. Novel processing of Ag-WC electrical contact materials using spark plasma sintering. *Materials & Design*. 2017;121:262-271.

- Slade PG, ed. *Electrical Contacts: Principles and Applications*. Boca Raton: CRC Press; 2014. 1210 p.
- Allen SE, Streicher E. The effect of microstructure on the electrical performance of Ag-WC-C contact materials. In: *Electrical Contacts - 1998. Proceedings of the Forty-Fourth IEEE Holm Conference on Electrical Contacts*; 1988 Oct 26-28; Arlington, VA, USA. p. 276-285.
- Slade P. Variations in Contact Resistance Resulting from Oxide Formation and Decomposition in Ag-W and Ag-WC-C Contacts Passing Steady Currents for Long Time Periods. *IEEE Transactions on Components, Hybrids, and Manufacturing Technology*. 1986;9(1):3-16.
- Yu H, Sun Y, Kesim MT, Harmon J, Potter J, Alpay SP, et al. Surface Degradation of Ag/W Circuit Breaker Contacts During Standardized UL Testing. *Journal of Materials Engineering and Performance*. 2015;24(9):3251-3262.
- Wang X, Fu C, Wang P, Yu H, Yu J. Hierarchically porous metastable β -Ag₂WO₄ hollow nanospheres: controlled synthesis and high photocatalytic activity. *Nanotechnology*. 2013;24(16):165602.
- Chen CC, Herhold AB, Johnson CS, Alivisatos AP. Size Dependence of Structural Metastability in Semiconductor Nanocrystals. *Science*. 1997;276(5311):398-401.
- Shukla S, Seal S, Vij R, Bandyopadhyay S, Rahman Z. Effect of Nanocrystallite Morphology on the Metastable Tetragonal Phase Stabilization in Zirconia. *Nano Letters*. 2002;2(9):989-993.
- Montini T, Gombac V, Hameed A, Felisari L, Adami G, Fornasiero P. Synthesis, characterization and photocatalytic performance of transition metal tungstates. *Chemical Physics Letters*. 2010;498(1-3):113-119.
- Takahashi T, Ikeda S, Yamamoto O. Solid-State Ionics-Solids with High Ionic Conductivity in the Systems Silver Iodide-Silver Oxyacid Salts. *Journal of the Electrochemical Society*. 1972;119(4):477-482.
- Zeng T, Yan H, Ning H, Zeng J, Reece MJ. Piezoelectric and Ferroelectric Properties of Bismuth Tungstate Ceramics Fabricated by Spark Plasma Sintering. *Journal of the American Ceramic Society*. 2009;92(12):3108-3110.
- Heyer O, Hollmann N, Klassen I, Jodlauk S, Bohatý L, Becker P, et al. A new multiferroic material: MnWO₄. *Journal of Physics: Condensed Matter*. 2006;18(39):L471.
- Andrés J, Gracia L, Gonzalez-Navarrete P, Longo VM, Avansi W Júnior, Volanti DP, et al. Structural and electronic analysis of the atomic scale nucleation of Ag on α -Ag₂WO₄ induced by electron irradiation. *Scientific Reports*. 2014;4:5391.
- Guo CX, Yu B, Xie JN, He LN. Silver tungstate: a single-component bifunctional catalyst for carboxylation of terminal alkynes with CO₂ in ambient conditions. *Green Chemistry*. 2015;17(1):474-479.
- Vafaezadeh M, Mahmoodi Hashemi M. One pot oxidative cleavage of cyclohexene to adipic acid using silver tungstate nano-rods in a Brønsted acidic ionic liquid. *RSC Advances*. 2015;5(40):31298-31302.
- Lin Z, Li J, Zheng Z, Yan J, Liu P, Wang C, et al. Electronic Reconstruction of α -Ag₂WO₄ Nanorods for Visible-Light Photocatalysis. *ACS Nano*. 2015;9(7):7256-7265.
- Zhang R, Cui H, Yang X, Tang H, Liu H, Li Y. Facile hydrothermal synthesis and photocatalytic activity of rod-like nanosized silver tungstate. *Micro & Nano Letters*. 2012;7(12):1285-1288.
- Xu D, Cheng B, Zhang J, Wang W, Yu J, Ho W. Photocatalytic activity of Ag₂MO₄ (M = Cr, Mo, W) photocatalysts. *Journal of Materials Chemistry A*. 2015;3(40):20153-20166.
- Pan L, Li L, Chen Y. Synthesis and electrocatalytic properties of microscaled Ag₂WO₄ and nanoscaled MWO₄ (M=Co, Mn). *Journal of Sol-Gel Science and Technology*. 2013;66(2):330-336.
- Cavalcante LS, Almeida MAP, Avansi W Jr., Tranquilin RL, Longo E, Batista NC, et al. Cluster Coordination and Photoluminescence Properties of α -Ag₂WO₄ Microcrystals. *Inorganic Chemistry*. 2012;51(20):10675-10687.
- Mondego M, de Oliveira RC, Penha M, Li MS, Longo E. Blue and red light photoluminescence emission at room temperature from CaTiO₃ decorated with α -Ag₂WO₄. *Ceramics International*. 2017;43(7):5759-5766.
- Longo E, Volanti DP, Longo VM, Gracia L, Nogueira IC, Almeida MAP, et al. Toward an Understanding of the Growth of Ag Filaments on α -Ag₂WO₄ and Their Photoluminescent Properties: A Combined Experimental and Theoretical Study. *The Journal of Physical Chemistry C*. 2014;118(2):1229-1239.
- Cheng L, Shao Q, Shao M, Wei X, Wu Z. Photoswitches of One-Dimensional Ag₂MO₄ (M = Cr, Mo, and W). *The Journal of Physical Chemistry C*. 2009;113(5):1764-1768.
- da Silva LF, Catto AC, Avansi W Jr., Cavalcante LS, Andrés J, Aguir K, et al. A novel ozone gas sensor based on one-dimensional (1D) α -Ag₂WO₄ nanostructures. *Nanoscale*. 2014;6(8):4058-4062.
- Longo VM, De Foggi CC, Ferrer MM, Gouveia AF, André RS, Avansi W, et al. Potentiated Electron Transference in α -Ag₂WO₄ Microcrystals with Ag Nanofilaments as Microbial Agent. *The Journal of Physical Chemistry A*. 2014;118(31):5769-5778.
- Dutta DP, Singh A, Ballal A, Tyagi AK. High Adsorption Capacity for Cationic Dye Removal and Antibacterial Properties of Sonochemically Synthesized Ag₂WO₄ Nanorods. *European Journal of Inorganic Chemistry*. 2014;2014(33):5724-5732.
- Roca RA, Sczancoski JC, Nogueira IC, Fabbro MT, Alves HC, Gracia L, et al. Facet-dependent photocatalytic and antibacterial properties of α -Ag₂WO₄ crystals: combining experimental data and theoretical insights. *Catalysis Science & Technology*. 2015;5(8):4091-4107.
- van den Berg AJ, Juffermans CAH. The polymorphism of silver tungstate Ag₂WO₄. *Journal of Applied Crystallography*. 1982;15:114-116.
- McKechnie JS, Turner LDS, Vincent CA, Bonino F, Lazzari M, Rivolta B. Silver mono-, di- and tetra-tungstates. *Journal of Inorganic and Nuclear Chemistry*. 1979;41(2):177-179.
- Skarstad PM, Geller S. (W₄O₁₆)₈-Polyion in the high temperature modification of silver tungstate. *Materials Research Bulletin*. 1975;10(8):791-799.
- Lemos PS, Altomare A, Gouveia AF, Nogueira IC, Gracia L, Llusar R, et al. Synthesis and characterization of metastable β -Ag₂WO₄: an experimental and theoretical approach. *Dalton Transactions*. 2016;45(3):1185-1191.

34. Beg MA, Jain A, Ghouse KM. Studies on silver tungstate-mercuric iodide reaction in solid state. *Journal of Solid State Chemistry*. 1988;75(1):1-6.
35. Jain A, Beg MA. Kinetics and mechanism of solid state reactions of silver tungstate with mercuric bromide and mercuric chloride. *Polyhedron*. 1995;14(15-16):2293-2299.
36. Sienko MJ, Mazumder BR. Some Solid State Studies of Silver-doped WO₃. *Journal of the American Chemical Society*. 1960;82(14):3508-3510.
37. Ng CHB, Fan WY. Preparation of highly uniform 1-dimensional a-Ag₂WO₄ nanostructures with controllable aspect ratio and study of the growth mechanism. *CrystEngComm*. 2016;18(41):8010-8019.
38. Pinatti IM, Nogueira IC, Pereira WS, Pereira PFS, Gonçalves RF, Varela JA, et al. Structural and photoluminescence properties of Eu³⁺ doped a-Ag₂WO₄ synthesized by the green coprecipitation methodology. *Dalton Transactions*. 2015;44(40):17673-17685.
39. Foggi CC, Fabbro MT, Santos LPS, de Santana YVB, Vergani CE, Machado AL, et al. Synthesis and evaluation of a-Ag₂WO₄ as novel antifungal agent. *Chemical Physics Letters*. 2017;674:125-129.
40. Cui X, Yu SH, Li L, Biao L, Li H, Mo M, et al. Selective Synthesis and Characterization of Single-Crystal Silver Molybdate/Tungstate Nanowires by a Hydrothermal Process. *Chemistry - A European Journal*. 2004;10(1):218-223.
41. de Santana YVB, Gomes JEC, Matos L, Cruvinel GH, Perrin A, Perrin C, et al. Silver Molybdate and Silver Tungstate Nanocomposites with Enhanced Photoluminescence. *Nanomaterials and Nanotechnology*. 2014;4:22.
42. da Silva LF, Catto AC, Avansi W Jr., Cavalcante LS, Mastelaro VR, Andrés J, et al. Acetone gas sensor based on a-Ag₂WO₄ nanorods obtained via a microwave-assisted hydrothermal route. *Journal of Alloys and Compounds*. 2016;683:186-190.
43. San-Miguel MA, da Silva EZ, Zanetti SM, Cilense M, Fabbro MT, Gracia L, et al. In situ growth of Ag nanoparticles on a-Ag₂WO₄ under electron irradiation: probing the physical principles. *Nanotechnology*. 2016;27(22):225703.
44. Assis M, Cordoncillo E, Torres-Mendieta R, Beltrán-Mir H, Mínguez-Vega G, Oliveira R, et al. Towards the scale-up of the formation of nanoparticles on a-Ag₂WO₄ with bactericidal properties by femtosecond laser irradiation. *Scientific Reports*. 2018;8:1884.
45. Rietveld HM. A profile refinement method for nuclear and magnetic structures. *Journal of Applied Crystallography*. 1969;2(2):65-71.
46. Ortiz AL, Cumbreira FL, Sánchez-Bajo F, Guiberteau F, Caruso R. Fundamental parameters approach in the Rietveld method: a study of the stability of results versus the accuracy of the instrumental profile. *Journal of the European Ceramic Society*. 2000;20(11):1845-1851.
47. Stephens PW. Phenomenological model of anisotropic peak broadening in powder diffraction. *Journal of Applied Crystallography*. 1999;32(Pt 2):281-289.
48. Toby BH. R factors in Rietveld analysis: How good is good enough? *Powder Diffraction*. 2006;21(1):67-70.
49. Shirley DA. High-Resolution X-Ray Photoemission Spectrum of the Valence Bands of Gold. *Physical Review B*. 1972;5(12):4709.
50. Pomerantsev AL, ed. *Progress in Chemometrics Research*. New York: Nova Science Publishers; 2005. 325 p.
51. Wang P, Huang B, Zhang Q, Zhang X, Qin X, Dai Y, et al. Highly Efficient Visible Light Plasmonic Photocatalyst Ag@Ag(Br,I). *Chemistry - A European Journal*. 2010;16(33):10042-10047.
52. Ho SF, Contarini S, Rabalais JW. Ion-beam-induced chemical changes in the oxyanions (Moyn-) and oxides (Mox) where M = chromium, molybdenum, tungsten, vanadium, niobium and tantalum. *The Journal of Physical Chemistry*. 1987;91(18):4779-4788.
53. Wanger CD, Riggs WM, Davis LE, Moulder JF; Muilenberg GE, ed. *Handbook of X-ray Photoelectron Spectroscopy*. Eden Prairie: Perkin-Elmer Corporation; 1979.
54. Vincent Crist B. *Handbooks of Monochromatic XPS Spectra - Volume 1 - The Elements and Native Oxides*. Mountain View: XPS International, LLC; 1999.
55. van Attekum PMTM, Trooster JM. Bulk- and surface-plasmon-loss intensities in photoelectron, Auger, and electron-energy-loss spectra of Mg metal. *Physical Review B*. 1979;20(6):2335.
56. Pollak RA, Ley L, McFeely FR, Kowalczyk SP, Shirley DA. Characteristic energy loss structure of solids from x-ray photoemission spectra. *Journal of Electron Spectroscopy and Related Phenomena*. 1974;3(5):381-398.
57. Hameed A, Ismail IMI, Aslam M, Gondal MA. Photocatalytic conversion of methane into methanol: Performance of silver impregnated WO₃. *Applied Catalysis A: General*. 2014;470:327-335.
58. Kaspar TC, Droubay T, Chambers SA, Bagus PS. Spectroscopic Evidence for Ag(III) in Highly Oxidized Silver Films by X-ray Photoelectron Spectroscopy. *The Journal of Physical Chemistry C*. 2010;114(49):21562-21571.
59. Hsu KC, Chen DH. Microwave-assisted green synthesis of Ag/reduced graphene oxide nanocomposite as a surface-enhanced Raman scattering substrate with high uniformity. *Nanoscale Research Letters*. 2014;9(1):193.
60. Fu J, Hou Y, Zheng M, Wei Q, Zhu M, Yan H. Improving Dielectric Properties of PVDF Composites by Employing Surface Modified Strong Polarized BaTiO₃ Particles Derived by Molten Salt Method. *ACS Applied Materials and Interfaces*. 2015;7(44):24480-24491.
61. Cole KS, Cole RH. Dispersion and Absorption in Dielectrics I. Alternating Current Characteristics. *The Journal of Chemical Physics*. 1941;9(4):341-351.
62. Cumming WA. The Dielectric Properties of Ice and Snow at 3.2 Centimeters. *Journal of Applied Physics*. 1952;23(7):768-773.